Journal Name

ARTICLE TYPE

Cite this: DOI: 10.1039/xxxxxxxxxx

Self-propulsion of catalytic nanomotors synthesised by seeded growth of asymmetric platinum-gold nanoparticles

Ibon Santiago[a], Luyun Jiang[b], John Foord [b*] and Andrew J. Turberfield[a*]

Received Date
Accepted Date

DOI: 10.1039/xxxxxxxxxx

www.rsc.org/journalname

Asymmetric bimetallic nanomotors are synthesised by seeded growth in solution, providing a convenient and high-throughput alternative to the usual top-down lithographic fabrication of self-propelled catalytic nanoparticles. These synthetic nanomotors catalyse H_2O_2 decomposition and exhibit enhanced diffusion that depends on fuel concentration, consistent with their chemical propulsion.

Self-propulsion has potential applications in many areas of nanoscience and technology, including drug delivery, chemical sensing and environmental remediation[1,2]. Progress in material science has facilitated the assembly of numerous self-propelled artificial devices with sizes in the nanometre to micrometre range[2–4]. Such motors operate at low Reynolds numbers at which inertia is negligible; they are propelled by self-generated chemical gradients that result from asymmetric catalytic reactions at the motor surface[5,6] and are sustained by fuel in the environment[7]. Asymmetry in catalysis is usually achieved through structural asymmetry in the motor. Asymmetric release of reaction products has been used to generate directed motion by self-diffusiophoresis[8] and self-electrophoresis[9] of particles over a range of different length scales and geometries, including Janus microparticles[5], bimetallic nanorods[10], sphere dimer nanomotors[11,12] and molecular nanomotors[13].

There have been many realizations of motors with dimensions of the order of micrometres or hundreds of nanometres[3]. However, the fabrication of even smaller synthetic motors, with dimensions of tens of nanometres or less, presents experimental challenges: at this length scale it is hard to create geometric anisotropy using the traditional top-down synthesis methods such as electron-beam lithography or physical vapour deposition[14]. Apart from recently reported enzymatic nanomotors[15,16], which exhibit increased diffusion when catalysing reactions of their substrates, 30 nm Pt/Au[9] and 40 nm Pt/mesoporous silica[17] Janus nanoparticles are the smallest current examples of synthetic, self-propelled nanomotors. For their production, symmetry breaking was achieved by shadow-growth physical vapour deposition of metallic catalyst and e-beam lithography, respectively.

Bimetallic nanoparticles with controlled shapes, sizes and compositions have been synthesised by various wet chemical methods[18–21]. Seeded growth, by reduction of a precursor metal salt on a metallic seed nanoparticle that provides a nucleation site, is a well-established method for the production of core-shell bimetallic nanoparticles[22,23]. The speed, extent and symmetry of the growth process can be tuned by controlling the ratio between the precursor and seed concentrations[19]. In this work we adapted such an approach to produce 15 nm asymmetric Pt-Au nanoparticles that behave as catalytic nanomotors. These asymmetric catalysts catalyse the decomposition of H_2O_2 and exhibit enhanced diffusion that depends on fuel concentration, consistent with self-propulsion. This approach for the fabrication of sub-100 nm nanomotors is significantly easier to implement than "top-down" synthesis methods and offers the possibility of high throughput.

We fabricated Pt-Au nanoparticles by seeded growth of Pt on Au nanoparticles (Figure 1, ESI Methods/Experimental M2). In order to obtain an asymmetric surface distribution of catalyst, a necessary condition for catalytic self-propulsion, we reduced the ratio of Pt precursor to seed allowing only partial surface coverage with Pt. Starting with a monodisperse solution of 15 nm diameter Au nanoparticles (Au NP) acting as seeds, platinum growth was achieved by adding K_2PtCl_4 followed by slow mixing with reducing agent $NaBH_4$. A change in the characteristic colour of Au NP was observed (from red to dark red) as the reaction took place.

[a] *Department of Physics, University of Oxford, Clarendon Laboratory, Parks Road, Oxford OX1 3PU, United Kingdom*
[b] *Department of Chemistry, University of Oxford , South Parks Road, Oxford, OX1 3TA, United Kingdom*
* *Andrew.Turberfield@physics.ox.ac.uk ,John.foord@chem.ox.ac.uk*
† Electronic Supplementary Information (ESI) available: [Description]. See DOI: 10.1039/b000000x/

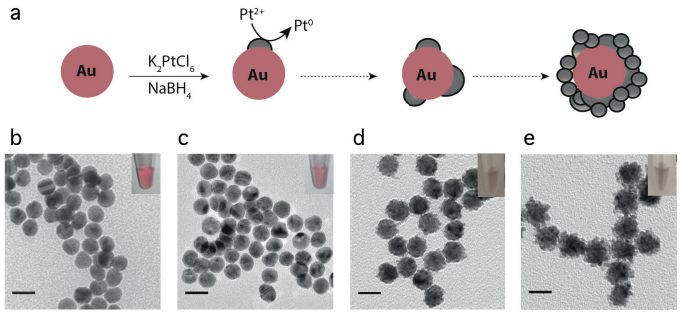

Fig. 1 *Chemical synthesis of Pt-Au nanoparticles.* (a) Scheme of Pt growth on 15 nm Au nanoparticles. (b-e) Transmission electron micrographs of Pt-Au nanoparticles obtained using 2.3 nM Au NP seeds (shown in b) and K_2PtCl_4 precursor concentrations of: c 0.1 mM, d 1mM and e 3mM. Micrographs show particles after drying by evaporation on carbon grids. Insets show the characteristic colours of the suspensions, turning from red (Au NP) to dark (thick layer core-shell Pt-Au NP). Sample c corresponds to asymmetric Pt-Au NP whose propulsive behaviour is studied in the text. Scale bars: 20 nm.

UV-vis spectroscopy showed that the absorption peak of gold decreased significantly (ESI Figure 1), which we associate with Pt growth on Au NP[24,25].

Figure 1 shows different stages of Pt on Au NP growth achieved by varying the Pt precursor concentration. TEM micrographs correspond to the Au NP seeds and samples reacted with 0.1 mM, 1 mM and 3 mM Pt precursor corresponding to ratios of Pt ion:Au atom of approximately 1:3, 10:3 and 30:3, respectively. As more Pt precursor is added, the morphology of the Pt-Au NP changes from a smooth surface with islands of Pt (Figure 1 c) to an uneven but approximately symmetrical thin layer core-shell Pt-Au NP (Figure 1 d) and, eventually, a thick layer core-shell structure (Figure 1 e). Nanoparticle size distributions determined from TEM micrographs and dynamic light scattering (DLS) (ESI Figure 2) confirm that the mean particle size increases with the concentration of Pt precursor. For the completely covered thick layer core-shell particles (Figure 1 e), both methods indicate an average 3 nm increase in radius. The most asymmetric surface distribution of Pt is observed for particles grown with 0.1 mM of Pt precursor (Figure 1 c): these putative asymmetric catalysts are named asymmetric Pt-Au NP hereafter.

We performed a control experiment by reacting the Pt precursor (3 mM) and reducing agent first and then mixing this solution with the 15 nm Au NP suspension. TEM micrographs (ESI Figure 4a and b) show that in this "physically mixed" control, smaller Pt NP are observed separately from Au NP which retain their initial, smooth shape with no evidence of significant surface growth. Similar mixtures, created by reducing an equivalent concentration of Pt precursor before adding Au NPs, were used as controls throughout this work.

The chemical composition of the particle surface was measured using X-ray photoelectron spectroscopy (XPS) (ESI Figure 3). After Pt deposition, peaks characteristic of both metallic Pt and Pt oxide are observed. For thicker Pt loadings, the signal from metallic Pt dominates. The Pt oxide peak is likely to arise from superficial oxidation in air prior to analysis.

To resolve the low coverages of Pt on the surface of asymmetric Pt-Au NP grown with 0.1 mM of Pt precursor is challenging using conventional TEM, although in some cases Pt clusters can be detected (ESI Figure 4c and d). We characterised the material composition of these asymmetric Pt-Au NP by high-angle annular dark field scanning transmission electron microscopy (HAADF-STEM) using elemental energy dispersive X-ray detection (EDX) to obtain better atomic contrast between Pt and Au as shown in Figure 2. EDX performed on single asymmetric Pt-Au NP confirmed the presence of crystalline Pt on the surface of Au NP (Figure 2a). Figure 2b shows background-subtracted signals characteristic of Pt and Au along a line scan across a particle, indicating an asymmetric distribution of Pt. Spatially resolved compositional analysis by EDX (Figure 2c, d) indicated the presence of three distinct surface types: pure Au, pure Pt and mixed Pt/Au. Although the EDX analysis cannot directly identify the metallic bond between Au and Pt the most likely interpretation of these observations and those described above is that Pt has grown directly on the Au NP.

Nanoparticle samples used for measurements of catalysis were filtered using a centrifuge filter (30 kDa MWCO Amicon filters, pore size 5 nm) to remove unreacted Pt salt and possible small

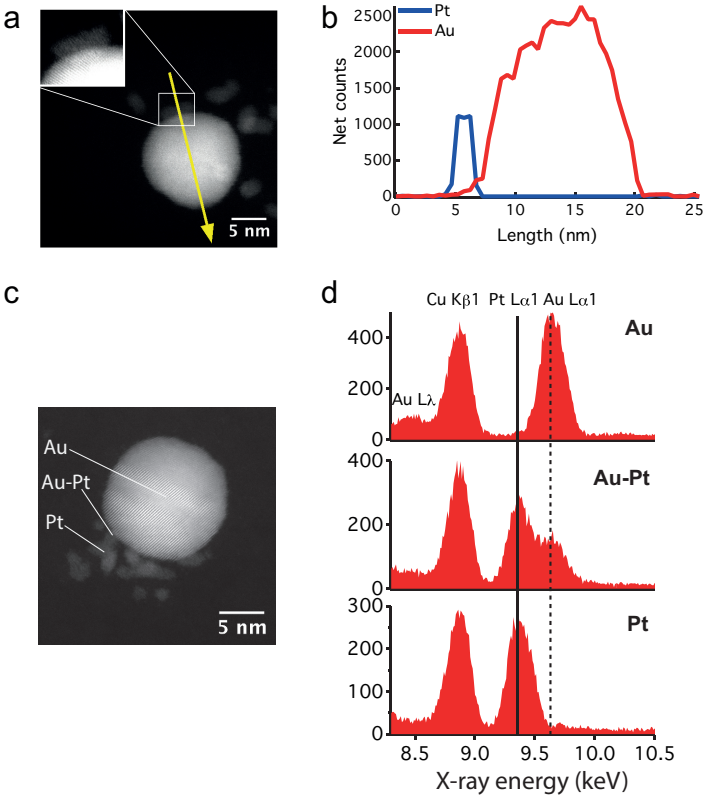

Fig. 2 *HAADF-STEM and energy-dispersive X-ray analysis of asymmetric Pt-Au NPs.* (a) Image of an asymmetric Pt-Au NP showing the line scan corresponding to the compositional analysis presented in b. Inset shows high resolution image of Pt on Au. (b) Compositional analysis, showing the net electron count (background substracted) along the line scan. (c) Representative HAADF-STEM micrograph with characteristic regions labelled. (d) Representative EDX point spectra centred around the Pt peak (solid line at 9.4 keV) and the Au peak (dashed line at 9.6 keV).

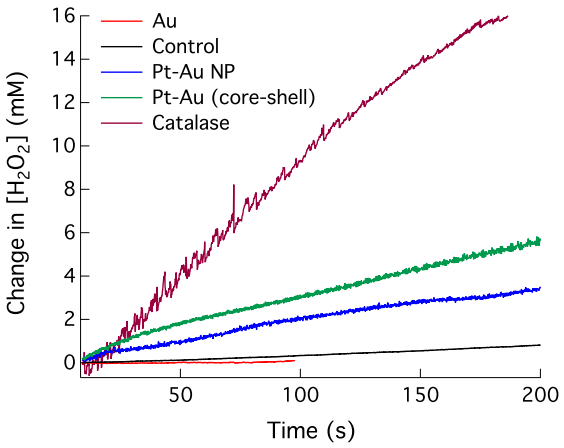

Fig. 3 *Electrochemical measurements of catalytic decomposition of H_2O_2.*The amperometric measurement was made using a Ag-coated glassy carbon electrode at a fixed potential of -0.6 V in solution of 25 mM H_2O_2 and 0.1 mM KCl at Ag-GCE with RDE (1300 rmp) after adding: 2.3 nM asymmetric Pt-Au NP; 1.2 nM thick layer core-shell Pt-Au NP; 0.25 nM catalase; 2.3 nM control solution (reduced Pt physically mixed with Au NP).

Pt NP formed in solution. Bubble formation was observed when H_2O_2 was added to a sample containing filtered nanoparticles but not when added to the filtrate.

To quantify the catalytic activity of asymmetric Pt-Au NP in solution we adapted an electrochemical method[26] (ESI Methods/Experimental M3). Catalytic nanoparticles (filtered by Amicon Filter, 30 kDa) were added to a 25 mM H_2O_2 solution and the change in concentration of H_2O_2 with time was measured using a H_2O_2 sensor (silver-coated glassy carbon electrode). A representative measurement is shown in ESI Figure 5 d. Changes of H_2O_2 concentration on addition of asymmetric Pt-Au NP and thick layer core-shell Pt-Au NP are plotted in Figure 3, together with controls and calibration measurements using catalase (ESI Figure 5). The sensor current shows no significant change on addition of uncoated Au NP. The rate of H_2O_2 decomposition in the presence of asymmetric Pt-Au NP is 9× higher that in the presence of the equivalent control solution (Au NP physically mixed with reduced Pt). An equivalent concentration of thick layer core-shell Pt-Au NP is 27× more catalytically active than the control. The significant catalytic activity observed, even for nanoparticles prepared with low Pt precursor concentrations (Figure 3), indicates that a large fraction of the Au NP are Pt-modified, consistent with the measured changes in optical absorption (ESI Figure 1), detection of Pt by HRTEM (ESI Figure 2), XPS (ESI Figure 3) and EDX (Figure 2), and the enhanced diffusion in the presence of H_2O_2 discussed below.

Motor activity can be assessed by measuring an enhancement of the effective diffusion coefficient of the catalytic particles in the presence of fuel. Here, the fuel is H_2O_2 , whose decomposition is catalysed by Pt. An asymmetric catalytic particle generates an asymmetric distribution of the product oxygen around the particle. The resulting propulsive force is attributed to a phoretic mechanism, whereby a self-generated gradient of oxygen concentration induces flow fields that propel the particle. In the case of other larger, bimetallic particles, self-electrophoresis has been proposed as the main mechanism for propulsion[9,27]. The nanoparticles studied here are subject to rapid rotational diffusion that randomises their direction of motion: nanomotor activity is observed in an increase in the apparent diffusion constant, $D_{eff} = D_0 + \frac{1}{3}V^2\tau$, where V is the ballistic velocity arising from catalytic activity and τ is the rotational diffusion time determined by the size of the particle[13]. Suitable methods for measuring the diffusion of nanometre-scale particles include microscopy tracking (nanoparticle tracking analysis, NTA), fluorescence correlation spectroscopy (FCS) and dynamic light scattering (DLS)[14]. For unlabelled metallic particles of 15 nm diameter, DLS is a suitable choice. Distributions of diffusion coefficients inferred by fitting DLS autocorrelation functions indicate a progressive increase in diffusivity of asymmetric Pt-Au NP with H_2O_2 concentration (Figure 4, SI Figure 6a). The apparent diffusion coefficient of asymmetric Pt-Au NP ($D_0 = 14.4 \pm 0.2\,\mu m^2\,s^{-1}$ in water) increases by approximately 30% with increasing H_2O_2 concentration until a plateau is reached at around 3% (v/v). No significant change in diffusivity on addition of H_2O_2 was observed for control solu-

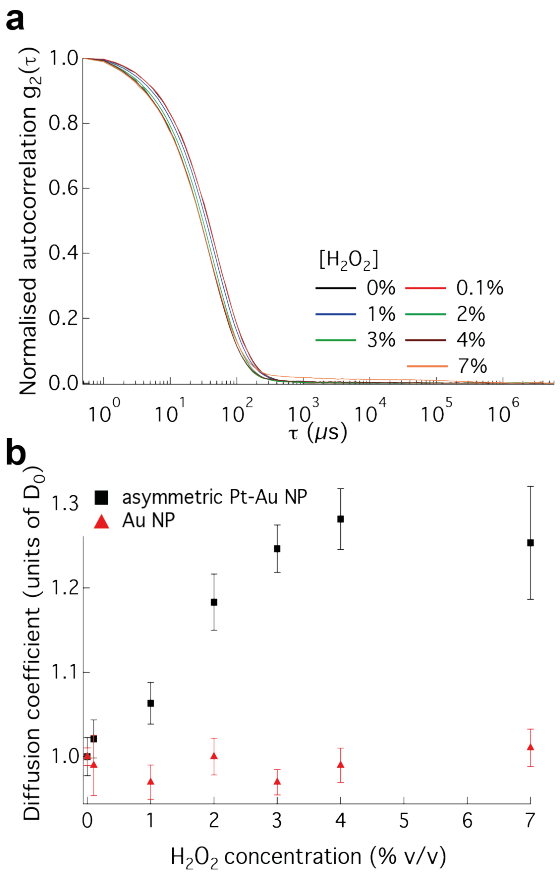

Fig. 4 *Dynamic light scattering measurement of motor activity of asymmetric Pt-Au NP.* DLS was used to measure the diffusion of 15 nm asymmetric Pt-Au NP at a range of hydrogen peroxide concentrations. (a) Normalised autocorrelation functions as a function of H_2O_2 concentration (%v/v). (b) Corresponding diffusion coefficients for asymmetric Pt-Au NPs (black, in units of $D_0 = 14.2\,\mu m^2\,s^{-1}$) and Au (black, in units of $D_0 = 14.4\,\mu m^2\,s^{-1}$) as a function of H_2O_2 concentration, averaged over 3 experimental runs (error bars indicate standard deviations).

tions of 15 nm Au NP, reduced Pt physically mixed with Au NP, or thick layer core-shell Pt-Au NPs (ESI Figure 7a). (As a result of the high catalytic activity of thick layer core-shell Pt-Au NP, the onset of bubbles at high concentrations of H_2O_2 interferes with the DLS measurement, producing autocorrelation functions with elevated baselines such as those shown in the inset to ESI Figure 7b; such data were automatically removed from the analysis.)

We used a viscous ionic liquid to increase the sensitivity of our measurements to changes in diffusivity. The use of viscous media to slow down the motion of self-propelled particles is common, especially when using tracking microscopy[9]. Asymmetric Pt-Au NP were mixed in 25% (v/v) of ionic liquid 1-Ethyl-3-methylpyridinium perfluorobutanesulfonate achieving a viscosity of approx. 20 cP at 20 °C (inferred from measurements of nanoparticle diffusion using DLS). In this medium we observe a twofold increase in diffusivity for 15 nm asymmetric Pt-Au NP when mixed with H_2O_2 (Figure 5). Comparable measurements on highly catalytic 5 nm Pt NP are shown in ESI Figure 8.

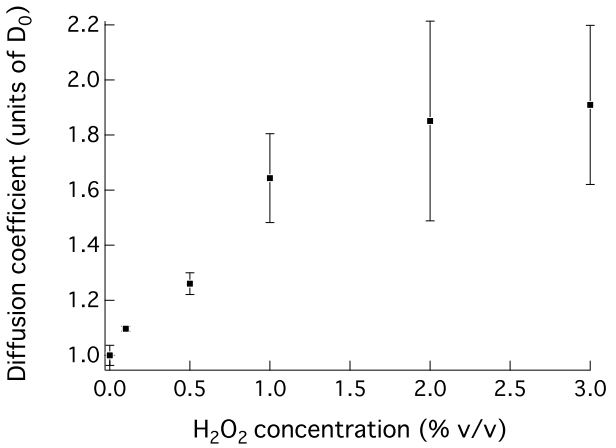

Fig. 5 *Dynamic Light Scattering measurement of motor activity of asymmetric Pt-Au NP in a viscous ionic liquid.* The diffusion coefficient for asymmetric Pt-Au NP (in units of $D_0 = 0.34\,\mu m^2\,s^{-1}$) is plotted as a function of H_2O_2 concentration, averaged over 3 experimental runs (error bars indicate standard deviations).

In summary, we have demonstrated a new wet-chemical approach to the synthesis of sub-100 nm asymmetric catalytic nanoparticles that function as nanomotors. In particular, we have grown Pt on the surface of Au NP by a seeded-growth method and characterised the resultant Pt-Au nanoparticles using HAADF-STEM, TEM, EDX, UV-vis absorption and XPS. Pt-Au nanoparticles synthesised with low Pt precursor concentration form asymmetric bimetallic nanoparticles. The development of a higher degree of control over nanoparticle morphology can be envisaged. The asymmetric Pt-Au nanoparticles catalyse the decomposition of hydrogen peroxide. We have used dynamic light scattering to demonstrate nanomotor activity of asymmetric particles in the presence of H_2O_2 fuel. Ballistic propulsion is manifest as an increase in the effective diffusion constant by up to 30% in hydrogen peroxide. This work paves the way to the high-throughput production of nanometre-scale active particles by wet-chemical methods. This may facilitate research into the practical applications of catalytic nanomotors, which remain an open scientific and technological challenge.

This work was funded by the Department of Education and Culture of the Basque Government (IS), Engineering and Physical Sciences Research Council grant EP/G037930/1, and a Royal Society-Wolfson Research Merit Award (AJT). We would like to thank Dr Neil Young (Department of Materials, University of Oxford) for assistance with STEM-EDX characterisation. We are grateful to Dr David Staunton (Biochemistry, University of Oxford) for access to DLS apparatus. We thank Prof. Richard Compton for helpful discussions.

There are no conflicts of interest to declare.

References

1 W. Gao and J. Wang, *Nanoscale*, 2014, **6**, 10486–10494.
2 J. Wang, *Nanomachines*, John Wiley & Sons, 2013.
3 S. J. Ebbens and J. R. Howse, *Soft Matter*, 2010, **6**, 726–738.
4 C. Bechinger, R. Di Leonardo, H. Löwen, C. Reichhardt, G. Volpe and G. Volpe, *Rev. Mod. Phys.*, 2016, **88**, 045006.
5 J. R. Howse, R. A. L. Jones, A. J. Ryan, T. Gough, R. Vafabakhsh and R. Golestanian, *Phys. Rev. Lett.*, 2007, **99**, 048102.
6 W. F. Paxton, S. Sundararajan, T. E. Mallouk and A. Sen, *Angew. Chem., Int. Ed.*, 2006, **45**, 5420–5429.
7 R. Kapral, *J. Chem. Phys.*, 2013, **138**, 020901–020911.
8 R. Golestanian, T. B. Liverpool and A. Ajdari, *Phys. Rev. Lett.*, 2005, **94**, 220801.
9 T.-C. Lee, M. Alarcón-Correa, C. Miksch, K. Hahn, J. G. Gibbs and P. Fischer, *Nano Lett.*, 2014, **14**, 2407–2412.
10 W. F. Paxton, K. C. Kistler, C. C. Olmeda, A. Sen, S. K. St Angelo, Y. Cao, T. E. Mallouk, P. E. Lammert and V. H. Crespi, *J. Am. Chem. Soc.*, 2004, **126**, 13424–13431.
11 L. F. Valadares, Y. G. Tao, N. S. Zacharia, V. Kitaev, F. Galembeck, R. Kapral and G. A. Ozin, *Small*, 2010, **6**, 565–572.
12 G. R uckner and R. Kapral, *Phys. Rev. Lett.*, 2007, **98**, 150603.
13 P. H. Colberg, S. Y. Reigh, B. Robertson and R. Kapral, *Acc. Chem. Res.*, 2014, **47**, 3504–3511.
14 M. Alarcón-Correa, D. Walker, T. Qiu and P. Fischer, *Eur. Phys. J. Spec. Top.*, 2016, **225**, 2241–2254.
15 C. Riedel, R. Gabizon, C. A. M. Wilson, K. Hamadani, K. Tsekouras, S. Marqusee, S. Presse and C. Bustamante, *Nature*, 2014, **517**, 227–230.
16 S. Sengupta, K. K. Dey, H. S. Muddana, T. Tabouillot, M. E. Ibele, P. J. Butler and A. Sen, *J. Am. Chem. Soc.*, 2013, **135**, 1406–1414.
17 X. Ma, K. Hahn and S. Sanchez, *J. Am. Chem. Soc.*, 2015, **137**, 4976–4979.
18 M. J. Bradley, C. G. Read and R. E. Schaak, *J. Phys. Chem. C*, 2015, **119**, 8952–8959.
19 J. He, M. T. Perez, P. Zhang, Y. Liu, T. Babu, J. Gong and Z. Nie, *J. Am. Chem. Soc.*, 2012, **134**, 3639–3642.
20 S. Mourdikoudis, M. Chirea, D. Zanaga, T. Altantzis, M. Mitrakas, S. Bals, L. M. Liz-Marzan, J. Pérez-Juste and I. Pastoriza-Santos, *Nanoscale*, 2015, **7**, 8739–8747.
21 S. I. Lim, M. Varon, I. Ojea-Jiménez, J. Arbiol and V. Puntes, *J. Mater. Chem.*, 2011, **21**, 11518–11523.
22 T. Yu, J. Zeng, B. Lim and Y. Xia, *Adv. Mater.*, 2010, **22**, 5188–5192.
23 S. Guo, J. Li, S. Dong and E. Wang, *J. Phys. Chem. C*, 2010, **114**, 15337–15342.
24 B. Du, O. Zaluzhna and Y. J. Tong, *Phys. Chem. Chem. Phys.*, 2011, **13**, 11568.
25 W. Wu, J. Li, S. Zou, J. Guo and H. Zhou, *Front. Mater. Sci.*, 2017, **11**, 42–50.
26 L. Jiang, J. Hu and J. S. Foord, *Electrochim. Acta*, 2015, **176**, 488–496.
27 Y. Wang, R. M. Hernandez, D. J. J. Bartlett, J. M. Bingham, T. R. Kline, A. Sen and T. E. Mallouk, *Langmuir*, 2006, **22**, 10451–10456.